Inorganic Chemistry

Article

pubs.acs.org/IC

Multifunctional One-Dimensional Rhodium(I)−Semiquinonato Complex: Substituent Effects on Crystal Structures and Solid-State Properties

Minoru Mitsumi,*[,†,‡] Shoji Ohtake,[†] Yuki Kakuno,[†] Yuuki Komatsu,[†] Yoshiki Ozawa,[†,‡] Koshiro Toriumi,[†,‡] Nobuhiro Yasuda,[§] Nobuaki Azuma,[∥] and Yuji Miyazaki[∥]

[†]Department of Material Science and [‡]Research Center for New Functional Materials, Graduate School of Material Science, University of Hyogo, 3-2-1 Kouto, Kamigori-cho, Ako-gun, Hyogo 678-1297, Japan

[§]Japan Synchrotron Radiation Research Institute/SPring-8, 1-1-1 Kouto, Sayo-cho, Sayo-gun, Hyogo 679-5198, Japan

[∥]Research Center for Structural Thermodynamics, Graduate School of Science, Osaka University, 1-1 Machikaneyama, Toyonaka, Osaka 560-0043, Japan

Supporting Information

ABSTRACT: Two new one-dimensional (1D) rhodium(I)−semiquinonato complexes formulated as $[Rh(3,6\text{-DBSQ-}4,5\text{-PDO})(CO)_2]_\infty$ (**4**; 3,6-DBSQ-4,5-PDO$^{\bullet-}$ = 3,6-di-*tert*-butyl-4,5-(1,3-propanedioxy)-1,2-benzosemiquinonato) and $[Rh(3,6\text{-DBSQ-}4,5\text{-}(N,N'\text{-DEN}))(CO)_2]_\infty$ (**5**; 3,6-DBSQ-4,5-$(N,N'$-DEN)$^{\bullet-}$ = 3,6-di-*tert*-butyl-4,5-(N,N'-diethylenediamine)-1,2-benzosemiquinonato) were synthesized to explore the nature of the unusual structural phase transition and magnetic and conductive properties recently reported for $[Rh(3,6\text{-DBSQ-}4,5\text{-}(MeO)_2)(CO)_2]_\infty$ (**3**; 3,6-DBSQ-4,5-$(MeO)_2^{\bullet-}$ = 3,6-di-*tert*-butyl-4,5-dimethoxy-1,2-benzosemiquinonato). Their crystal structures and magnetic and conductive properties were investigated. Compounds **4** and **5** comprise neutral 1D chains of complex molecules stacked in a staggered arrangement with fairly short average Rh−Rh distances of 3.06 Å for **4** and 3.10 Å for **5**. These distances are similar to those for **3** (3.09 Å); however, the molecules of **5** are strongly dimerized in the 1D chain. Compound **4** undergoes a first-order phase transition at T_{trs} = 229.1 K, and its magnetic properties drastically change from antiferromagnetic coupling in the room-temperature (RT) phase to strong ferromagnetic coupling in the low-temperature (LT) phase. In addition, compound **4** exhibits a long-range ordering of net magnetic moments originating from the imperfect cancellation of antiferromagnetically coupled spins between the ferromagnetic 1D chains at T_N = 10.9 K. Furthermore, this compound exhibits an interesting crossover from a semiconductor with a small activation energy (E_a = 31 meV) in the RT phase to a semiconductor with a large activation energy (E_a = 199 meV) in the LT phase. These behaviors are commonly observed for **3**. Alternating current susceptibility measurements of **4**, however, revealed a frequency-dependent phenomenon below 5.2 K, which was not observed for **3**, thus indicating a slow spin relaxation process that possibly arises from the movements of domain walls. In contrast, compound **5**, which possesses a strongly dimerized structure in its 1D chain, shows no sign of strong ferromagnetic interactions and is an insulator, with a resistivity greater than 7 × 10^7 Ω cm.

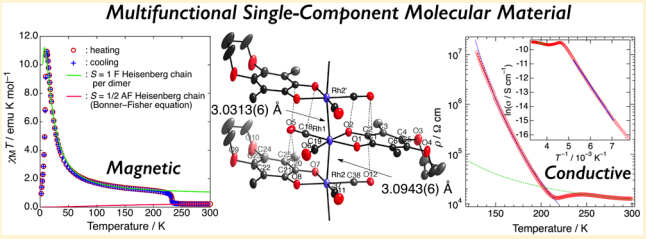

1. INTRODUCTION

The exploration of molecular materials that exhibit multifunctionalities such as magnetic, electrical, dielectric, or optical properties is an important and challenging theme in materials science.[1−6] To realize such multifunctional molecular materials, multicomponent systems are favorable because they allow each component to possess different physical properties. However, given the importance of a mutual interplay or synergy between these physical properties, the utilization of a single-component molecule is considered to be more advantageous. Multifunctional single-component systems that exhibit both magnetic and conductive properties have been reported thus far, many of which have been constructed using spiro-conjugated biphenalenyl radicals,[7] bisthiaselenazolyl radicals,[8,9] or extended tetrathiafulvalene (TTF) dithiolene complexes[10] as the building blocks.

To develop new multifunctional single-component molecular materials that exhibit both magnetic and electrical properties, we have pursued the design and synthesis of a series of one-dimensional (1D) rhodium(I)−semiquinonato complexes with a linear rhodium chain based on $[Rh(3,6\text{-DBSQ})(CO)_2]_\infty$ (**1**; 3,6-DBSQ$^{\bullet-}$ = 3,6-di-*tert*-butyl-1,2-benzosemiquinonato).[11,12] Semiquinonate is an organic radical anion with $S = {}^1/_2$ and is one of the redox series of dioxolene that can produce three redox isomers of benzoquinone (BQ), semiquinonate ($SQ^{\bullet-}$), and catecholate (Cat^{2-}). Furthermore, metal−dioxolene

Received: August 11, 2014
Published: October 21, 2014

 © 2014 American Chemical Society dx.doi.org/10.1021/ic5019532 | *Inorg. Chem.* 2014, 53, 11710−11720

complexes with very close energy levels between the frontier orbitals of the metal d and dioxolene π^* orbitals can undergo intramolecular charge transfer between the metal and ligand, the so-called valence tautomerism.[13−15] The semiquinonato radical ligand in our target system can serve not only as a spin carrier of $S = {}^1/_2$ but also as an electron acceptor for the partial oxidization of a rhodium(I) linear chain that produces a conducting 1D d band. In our pursuit to develop multifunctional single-component molecular materials, we have thus far reported two members of the family of 1D rhodium−dioxolene complexes: 1D mixed-valence rhodium(I,II)−semiquinonato/catecholato complex $[Rh(3,6\text{-DBDiox-4,5-Cl}_2)(CO)_2]_\infty$ (**2**; 3,6-DBDiox-4,5-Cl_2 = 3,6-di-*tert*-butyl-4,5-dichloro-1,2-benzosemiquinonato or 3,6-di-*tert*-butyl-4,5-dichlorocatecholato)[16] and 1D rhodium(I)−semiquinonato complex, $[Rh(3,6\text{-DBSQ-4,5-(MeO)}_2)(CO)_2]_\infty$ (**3**; 3,6-DBSQ-4,5-$(MeO)_2^{\bullet-}$ = 3,6-di-*tert*-butyl-4,5-dimethoxy-1,2-benzosemiquinonato).[17,18] Compounds **2** and **3** comprise neutral 1D chains of complex molecules stacked in a staggered arrangement with average Rh−Rh distances of 2.88 Å for **2** and 3.09 Å for **3**, which are considerably shorter than that for **1** (3.28 Å). In the former case, the Rh(I,II)−semiquinonato/catecholato mixed-valence state was realized by introducing two electron-withdrawing chloro substituents at the 4 and 5 positions of the 3,6-$DBSQ^{\bullet-}$ ligand to adjust the energy level of the vacant semiquinonato ligand π^* orbital to that of the filled 1D d band; consequently, the compound is a paramagnetic semiconductor with a significantly higher electrical conductivity of σ_{RT} = 17−34 S cm^{-1} at room temperature.[16] In contrast, we observed the latter compound **3** to exhibit unprecedented bistable multifunctionality with respect to its magnetic and conductive properties in the temperature range 228−207 K. The observed bistability results from thermal hysteresis arising from a first-order phase transition. The 1D chains in **3** are connected three-dimensionally by interchain C−H···O hydrogen bonds between methoxy groups of semiquinonato ligands, and the transition induces a drastic structural change accompanying the exchange of the C−H···O hydrogen-bond partners between the semiquinonato ligands. The complex molecules are strongly overlapped, leading to unusually strong ferromagnetic interactions in the low-temperature (LT) phase (J/k_B = +74(1) K, g = 2.67(2), and zJ'/k_B = −1.98(3) K if the alternately stacked neighboring complex molecules in the 1D chain are assumed to have formed triplet dimers), which change to antiferromagnetic interactions (J/k_B = −163(3) K with g fixed at 2.00) in the room-temperature (RT) phase with hysteresis. In addition, compound **3** exhibits long-range antiferromagnetic ordering between the ferromagnetic chains and spontaneous magnetization at a transition temperature T_N of 14.2 K because of spin canting (i.e., canted antiferromagnetism). The electrical conductivity of **3** measured using a single crystal is 4.8 × 10^{-4} S cm^{-1} at 300 K, which is relatively high despite Rh not being in a mixed-valence state. Furthermore, this compound exhibits an unusual change in thermally activated conductive behavior from a small activation energy (E_a = 88 meV) in the RT phase to a large activation energy (E_a = 386 meV) in the LT phase. However, such unusual magnetic and conductive behaviors were only observed in the case of compound **3**, and density functional theory (DFT) calculations based on cluster models could not reproduce the strong ferromagnetic interaction observed for compound **3**.

Further exploration of the nature of these unusual properties observed for **3** requires the synthesis of new chemically modified compounds and systematic investigation of the influence of the chemical modifications on their crystal structures and magnetic and conductive properties. In particular, the presence of two ether oxygen atoms at the 4 and 5 positions of the 3,6-$DBSQ^{\bullet-}$ ligand in **3** is believed to result in strong ferromagnetic interactions. Thus, we decided to investigate two chemically modified 1D rhodium(I)−semiquinonato complexes in which two methoxy groups at the 4 and 5 positions (*O,O*-substitutions) in 3,6-DBSQ-$(OMe)_2^{\bullet-}$ ligand are replaced by 1,3-propanedioxy (*O,O*-substitutions) and *N,N*′-diethylenediamine (*N,N*-substitutions) groups, respectively. We herein report the syntheses, crystal structures, and solid-state properties of two new families of 1D rhodium(I)−semiquinonato complexes: $[Rh(3,6\text{-DBSQ-4,5-PDO})(CO)_2]_\infty$ (**4**; 3,6-DBSQ-4,5-$PDO^{\bullet-}$ = 3,6-di-*tert*-butyl-4,5-(1,3-propanedioxy)-1,2-benzosemiquinonato) and $[Rh(3,6\text{-DBSQ-4,5-}(N,N'\text{-DEN}))(CO)_2]_\infty$ (**5**; 3,6-DBSQ-4,5-$(N,N'\text{-DEN})^{\bullet-}$ = 3,6-di-*tert*-butyl-4,5-(*N,N*′-diethylenediamine)-1,2-benzosemiquinonato) (Chart 1). We observed that compound

Chart 1

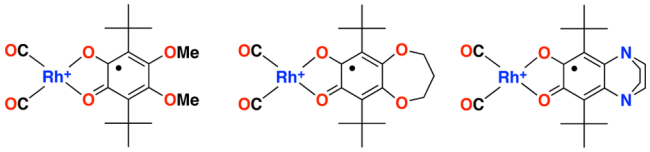

3 **4** **5**

4 with the *O,O*-substitutions undergoes a first-order phase transition at T_{trs} = 229.1 K and exhibits a drastic change in magnetic properties from antiferromagnetic coupling in the RT phase to strong ferromagnetic coupling in the LT phase, although this compound does not exhibit a significant hysteresis. This compound also shows a remarkable change in thermally activated conductive behavior from a small activation energy in the RT phase to a large activation energy in the LT phase. These behaviors are similar to those observed for **3**. The ac susceptibility of **4**, however, exhibits a frequency-dependent phenomenon below 5.2 K, which was not observed for **3**, thus indicating a slow spin relaxation process that possibly arises from the movements of domain walls. In contrast, compound **5** with the *N,N*-substitutions, in which complex molecules are strongly dimerized in the 1D chain, exhibits no sign of such a strong ferromagnetic interaction and is an insulator, with resistivity greater than 7 × 10^7 Ω cm.

2. EXPERIMENTAL SECTION

2.1. General Procedures and Materials. All syntheses were performed using standard vacuum line and Schlenk techniques under an argon atmosphere. All solvents were dried using appropriate drying agents and were freshly distilled under argon before use.[19] Dodecacarbonyltetrarhodium(0) ($[Rh_4(CO)_{12}]$),[20] 3,6-di-*tert*-butyl-1,2-benzoquinone (3,6-DBBQ),[21] and 3,6-di-*tert*-butyl-4,5-(*N,N*′-diethylenediamine)-1,2-benzoquinone (3,6-DBBQ-4,5-(*N,N*′-DEN))[22] were prepared according to the literature procedures.

2.2. Syntheses. *3,6-Di-tert-butyl-4,5-(1,3-propanedioxy)-1,2-benzoquinone (3,6-DBBQ-4,5-PDO).* This compound was synthesized using a procedure similar to that reported in the literature.[23] To a solution of 3,6-di-*tert*-butyl-1,2-benzoquinone (3,6-DBBQ) (1.125 g, 5.11 mmol) dissolved in 20 mL of DMF were added 1,3-propanediol (4.3 mL, 59 mmol), MnO_2 (54 mg, 0.62 mmol) that was well ground with a mortar and pestle, and NaOH (41 mg, 1.0 mmol). The reaction mixture was heated to 40 °C and stirred for 5 h, whereupon the color of the reaction mixture became dark red. After removal of any

dx.doi.org/10.1021/ic5019532 | Inorg. Chem. 2014, 53, 11710−11720

Table 1. Details of the Crystallographic Data Collection, Structural Determination, and Refinement for Compounds 4 and 5

	4 in the RT phase	4 in the LT phase	5 at 250 K
formula	$C_{19}H_{24}O_6Rh$	$C_{19}H_{24}O_6Rh$	$C_{20}H_{26}N_2O_4Rh$
fw	451.29	451.29	461.34
T, K	240	180	250
cryst size, mm^3	0.395 × 0.050 × 0.025	0.395 × 0.050 × 0.025	0.100 × 0.012 × 0.010
wavelength, Å	0.5603	0.5603	0.830 77
cryst syst	monoclinic	monoclinic	triclinic
space group	$P2_1/n$	$P2_1/n$	$P\bar{1}$
a, Å	6.1120(10)	6.0060(10)	6.1926(4)
b, Å	29.3860(10)	29.3360(10)	16.3109(10)
c, Å	21.7000(10)	21.6430(10)	21.7617(16)
α, deg			110.0354(16)
β, deg	93.857(2)	94.592(3)	97.032(2)
γ, deg			93.212(2)
V, Å^3	3888.6(7)	3801.1(7)	2038.2(2)
Z	8	8	4
D_c, g cm^{-1}	1.542	1.577	1.503
μ, mm^{-1}	0.447	0.458	1.234
$F(000)$	1848	1848	948
θ_{max}, θ_{min}, deg	23.595, 2.641	23.613, 2.840	30.029, 1.178
no. total reflns	30 604	25 256	11 792
no. unique reflns	10 527	9779	6230
R_{int}	0.0378	0.0461	0.0391
no. obsd [$I > 2\sigma(I)$]	8135	8572	4467
$R1$, $wR2$ [$I > 2\sigma(I)$]	0.0417	0.0477	0.0493
$R1$, $wR2$ (all data)	0.1187	0.1340	0.1522
GOF	1.081	1.138	1.057
max, min $\Delta\rho$, e Å^{-3}	0.492, −0.947	0.629, −0.605	0.568, −0.725

insoluble material by suction filtration, the filtrate was diluted with 300 mL of 5% sodium chloride solution and then extracted with dichloromethane (100 mL × 3). The combined organic extracts were evaporated to dryness in vacuo at 50 °C. The mixture was purified by column chromatography (silica gel, *n*-hexane/diethyl ether 1:1 v/v, R_f = 0.51) to afford the desired product. The product was further purified by recrystallization from hexane at −78 °C to yield red crystals of pure 3,6-DBBQ-4,5-PDO (284 mg, 971 μmol, 19% yield). ^{1}H NMR (600 MHz, $CDCl_3$, ppm): δ 1.31 (s, 18H, *t*-butyl), 2.23 (quin, 2H, J = 5.8 Hz, $-CH_2-CH_2-CH_2-$), 4.25 (t, 4H, J = 5.8 Hz, $-O-CH_2-CH_2-$). Anal. Calcd for $C_{17}H_{24}O_4$: C, 69.84; H, 8.27; O, 21.89. Found: C, 69.79; H, 8.27; O, 21.82.

[Rh(3,6-DBBQ-4,5-PDO)(CO)$_2$]$_\infty$ (**4**). $[Rh_4(CO)_{12}]$ (57.6 mg, 77.0 μmol) and 3,6-DBBQ-4,5-PDO (88.2 mg, 302 μmol) were dissolved in 7 mL of toluene/*n*-hexane (5:21, v/v) at 35 °C. The mixture was stirred at 35 °C for 10 min and was subsequently filtered using a PTFE cannula fitted with a glass-fiber filter. After being maintained at 35 °C, the filtrate was gradually cooled to −10 °C over a period of 20 h using a refrigerated thermostatic bath. The resulting dark-brown fine needle-like crystals were collected by suction filtration and were rinsed with ice-cooled *n*-hexane. Yield: 75.2 mg, 166 μmol (55%). Anal. Calcd for $C_{19}H_{24}O_6Rh$: C, 50.57; H, 5.36. Found: C, 50.78; H, 5.48.

[Rh(3,6-DBBQ-4,5-(N,N′-DEN))(CO)$_2$]$_\infty$ (**5**). $[Rh_4(CO)_{12}]$ (54.9 mg, 73.4 μmol) and 3,6-DBBQ-4,5-(*N*,*N*′-DEN) (109.5 mg, 362 μmol) were dissolved in 5 mL of a mixed solvent of toluene/*n*-hexane (1:1, v/v) at 50 °C. The mixture was stirred at 50 °C for 10 min and was subsequently filtered using a PTFE cannula fitted with a glass-fiber filter. After being maintained at 50 °C, the filtrate was gradually cooled to 0 °C over 20 h using a refrigerated thermostatic bath. The resulting dark-brown fine needle-like crystals were collected by suction filtration and were rinsed with ice-cooled *n*-hexane. Yield: 31.7 mg, 68.7 μmol (23%). Anal. Calcd for $C_{20}H_{26}N_2O_4Rh$: C, 52.07; H, 5.68; N, 6.07. Found: C, 51.94; H, 5.64; N, 5.94.

2.3. Physical Measurements. Elemental analyses were performed at the Center for Organic Elemental Microanalysis of the Graduate School of Pharmaceutical Sciences, Kyoto University. ^{1}H NMR spectra were obtained on a JEOL ECA-600 spectrometer using tetramethylsilane (TMS) as an internal standard. DSC measurements were performed with a PerkinElmer Diamond DSC at a scanning rate of 5 K min^{-1} using helium as the purge gas. Heat-capacity measurements were performed in the temperature range 8−312 K with a laboratory-made low-temperature adiabatic calorimeter for small samples.[24] The sample of 0.149 04 g after buoyancy correction was loaded into a gold-plated copper cell and sealed under helium gas at ambient pressure using an indium gasket. The helium gas functions as a heat-exchange medium. Thermometry was performed with a rhodium−iron alloy resistance thermometer (nominal 27 Ω, Oxford Instruments) calibrated on the basis of the international temperature scale of 1990 (ITS-90). UV−vis−NIR spectra of the compounds dispersed in KBr pressed disks were recorded on a Hitachi U-3500 spectrophotometer equipped with a 60 mm internal diameter integrating-sphere apparatus. FT-IR spectra were recorded on a JASCO FT/IR-4100 spectrophotometer using samples pressed into KBr disks. Magnetic measurements of the compounds were performed using a Quantum Design MPMS-5SH or MPMS-XL7 SQUID magnetometer. Polycrystalline samples of **4** (44.35 mg) and **5** (28.89 mg) held in a polyethylene film inside a plastic straw were used. Direct current susceptibility measurements were performed in the temperature range 2−300 K under the dc fields mentioned in the corresponding figures and text. Field-dependent dc magnetizations were measured in magnetic fields up to 50 kOe in the temperature range 2−25 K. Alternating current measurements on the polycrystalline sample were performed at frequencies of 1, 10, 99.9, 499, and 997 Hz with an ac-field amplitude of 2 Oe with zero dc bias field. The molar magnetic susceptibility (χ_M) was obtained after subtraction of the calculated diamagnetic core contribution estimated from Pascal's constants and the measured diamagnetic contribution of the polyethylene film and plastic straw. Temperature dependences of the electrical resistivity of the compressed pellets of the compounds were measured with an Agilent 4284A precision LCR meter and a closed-cycle helium refrigerator (Iwatani, CryoMini D105) using a pseudo-four-probe ac method (100 Hz).

dx.doi.org/10.1021/ic5019532 | Inorg. Chem. 2014, 53, 11710−11720

2.4. Synchrotron Radiation X-ray Crystallography. A single crystal of $[Rh(3,6\text{-DBBQ-}4,5\text{-PDO})(CO)_2]_\infty$ (**4**) was mounted onto carbon fibers, and the crystal was attached to a closed-cycle helium cryostat. Diffraction data were collected at 240 and 180 K under vacuum conditions (2.0×10^{-3} Pa) using Si(111)-monochromated synchrotron radiation (0.5603 Å) and a MAC Science low-temperature vacuum X-ray camera equipped with an imaging plate area detector at the BL02B1 beamline of SPring-8. Reflections of each frame were indexed and integrated using DENZO and were subsequently scaled using SCALEPACK.[25] An empirical correction for absorption anisotropy was applied to all intensity data using PLATON-MULABS.[26] The diffraction data for $[Rh(3,6\text{-DBBQ-}4,5\text{-}(N,N'\text{-DEN}))(CO)_2]_\infty$ (**5**) were collected on a high-precision diffractometer with Si(111)-monochromated synchrotron radiation (0.830 77 Å) with Rigaku Saturn 724 CCD detector at the SPring-8 BL40XU beamline.[27,28] Lorentz, polarization, and an empirical absorption correction based on Fourier series approximation were applied to the intensity data. The structures of **4** and **5** were solved by direct methods (SIR97)[29] and were expanded using Fourier techniques. All refinements were made on F^2 by a full-matrix least-squares method using the SHELXL-2014 program.[30] The X-ray analyses were performed using the free GUI software Yadokari-XG.[31,32] All non-hydrogen atoms in **4** and **5** were refined anisotropically, whereas hydrogen atoms were placed at their geometrically calculated positions and refined isotropically with fixed U values using a riding model. All crystallographic data and structure refinement results for these compounds are reported in Table 1.

3. RESULTS AND DISCUSSION

3.1. Heat Capacity. The heat capacity of compound **4** was measured by adiabatic calorimetry (Figure 1). A sharp thermal anomaly with a tail on the low-temperature side down to ca. 200 K was observed at T_{trs} = 229.1 K during heating; this anomaly is assigned to a first-order phase transition on the basis of its sharp peak shape, although supercooling was scarcely observed during the cooling process. The observed thermal anomaly indicates the presence of room-temperature (RT) and low-temperature (LT) phases. The excess enthalpy and entropy of the phase transition were determined to be 1.501(17) kJ mol^{-1} and 6.632(79) J K^{-1} mol^{-1}, respectively. Even if the observed entropy originates from the $S = {}^1/_2$ spins of the semiquinonato ligands alone, the actual entropy acquisition is larger than the maximum entropy gain $\Delta S = R \ln 2 = 5.76$ J K^{-1} mol^{-1}, which is expected for an $S = {}^1/_2$ spin state. In this compound, the distinct structural disorder that would contribute to the entropy gain was not apparently observed. A similar tendency was already observed in compound **3**, in which the changes in intramolecular and lattice vibrations are considered to contribute to the excess entropy, in addition to certain contribution from the $S = {}^1/_2$ spins.[17] Therefore, not only certain contributions from the $S = {}^1/_2$ spins but also similar changes in the intramolecular and lattice vibrations would contribute to the excess entropy observed in **4**. On the other hand, the DSC results for compound **5** did not show any latent heat in the measured temperature range 303−94 K.

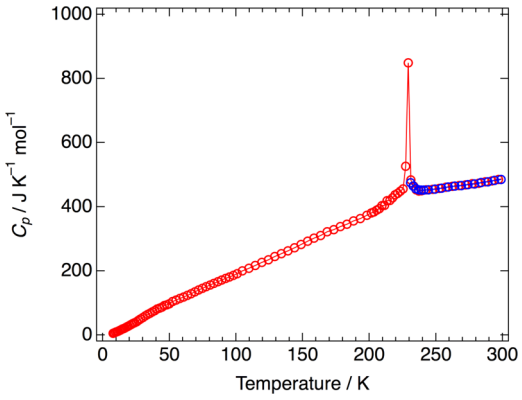

Figure 1. Molar heat capacity of $[Rh(3,6\text{-DBSQ-}4,5\text{-PDO})(CO)_2]_\infty$ (**4**) as a function of temperature. Red circles represent the data obtained by a heating process after the sample was cooled to 8 K. Blue circles represent the data obtained after the sample was cooled to 231.0 K; these data did not show supercooling of the RT phase.

3.2. Crystal Structures. Crystal structures of very small needle crystals of compounds **4** and **5** were determined by synchrotron X-ray crystallographic analyses because attempts to grow sufficiently large single crystals of these compounds for X-ray diffraction experiments in the laboratory system were unsuccessful.

$[Rh(3,6\text{-DBSQ-}4,5\text{-PDO})(CO)_2]_\infty$ (4). The crystal structures of **4** in the RT and LT phases belong to the same monoclinic space group $P2_1/n$ as those of compound **3**; the 1D chain structures and crystal structures in both phases are shown in Figure 2 and Supporting Information Figures S1−S4, respectively. Selected bond lengths for both phases are listed in Supporting Information Table S1.

The crystal consists of neutral 1D chains of planar $Rh(3,6\text{-DBSQ-}4,5\text{-PDO})(CO)_2$ units stacked in a staggered arrangement along the a-axis, where the twisting angle between adjacent molecules estimated from the torsion angles of O1−Rh1−Rh2−O7 and O2−Rh1−Rh2−O8 is ca. 140° at 240 K in the RT phase. The Rh1−Rh2 and Rh1−Rh2* distances are 3.0943(6) and 3.0313(6) Å, respectively, which are 0.215 Å shorter than those of $[Rh(3,6\text{-DBSQ})(CO)_2]_\infty$ (**1**) (3.252(4) and 3.304(5) Å at 294−297 K)[11] on average and are almost the same as those of $[Rh(3,6\text{-DBSQ-}4,5\text{-}(MeO)_2)(CO)_2]_\infty$ (**3**) (3.0796(4) and 3.1045(4) Å at 226 K).[17] The bond angles of Rh2−Rh1−Rh2* and Rh1−Rh2−Rh1′ are both 172.37(1)°, resulting in a slightly folded zigzag Rh−Rh chain structure. Eight types of intermolecular C···O contacts less than the sum of their respective van der Waals radii (3.22 Å) exist between the neighboring semiquinonato ligands and carbonyl ligands in the stacked molecules (3.066(3)−3.200(4) Å); they are represented by dashed lines in Figure 2a. The slight zigzag conformation observed in the Rh−Rh chain is considered to be due to the influence of these intermolecular interactions. The oxidation state in a dioxolene ligand can generally be estimated from its C−O distances because the C−O distances in the semiquinonate and catecholate states are known to be 1.29(1) and 1.35(1) Å, respectively.[33] The average C−O distance of the dioxolene ligand in **4** is 1.309(5) Å, and the six-membered C−C rings also exhibit a quinoid-type distortion: an average of 1.373(5) Å for two alternating short C−C bonds and an average of 1.429(8) Å for four longer C−C bonds. These structural features indicate that the dioxolene ligands in **4** are coordinated to diamagnetic rhodium(I) ions as a semiquinonate state. The 1,3-propanedioxy moieties of the semiquinonato ligands in the 1D chain are bent out of the molecular plane in the same direction so as to fill the vacant spaces formed by the overlap of the neighboring semiquinonato and carbonyl ligands. The 1,3-propanedioxy moiety of the semiquinonato ligand coordinated to the Rh1 atom exhibits significantly larger thermal ellipsoids corresponding to large-amplitude thermal motion of these atoms. Intermolecular C···O distances between the 1,3-propanedioxy moieties of adjacent 1D chains are relatively short (O3···C34 = 3.570(6), O9···C15

dx.doi.org/10.1021/ic5019532 | Inorg. Chem. 2014, 53, 11710−11720

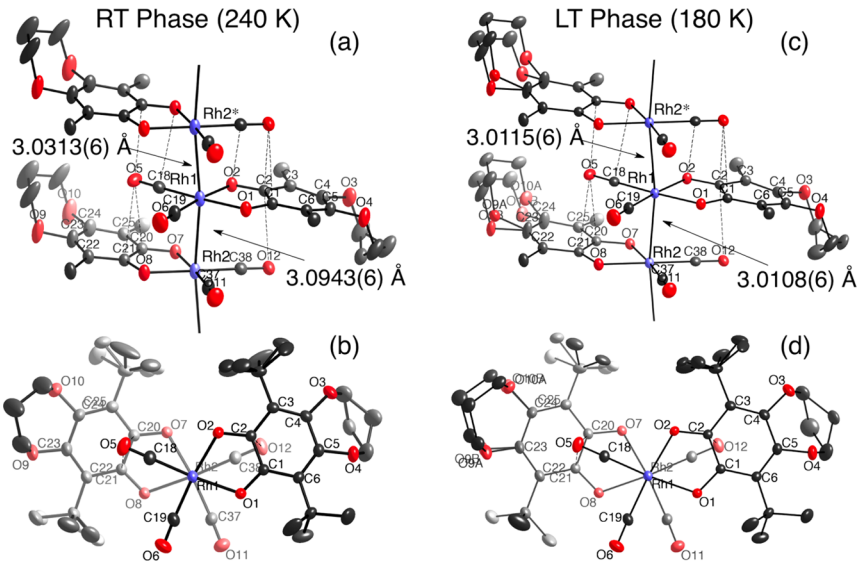

Figure 2. Crystal structures of $[Rh(3,6\text{-DBSQ-}4,5\text{-PDO})(CO)_2]_\infty$ (**4**). (a) Structure of the infinite chain built from a stack of complex molecules and (b) structural view down the Rh−Rh axis showing an overlap mode of the complex molecules in the RT phase (240 K). Symmetry operation: * 1 + *x*, *y*, *z*. (c) Structure of an infinite chain and (d) a structural view down the Rh−Rh axis in the LT phase (180 K). Intermolecular C···O contact distances less than the sum of their respective van der Waals radii (3.22 Å) are represented by dashed lines. Methyl carbon atoms of *t*-Bu groups are omitted in parts a and c for clarity.

= 3.603(5) Å), indicating that the adjacent 1D chains are connected two-dimensionally parallel to the *ab* plane by the weak C−H···O hydrogen bonds, as shown in Supporting Information Figures S1 and S2, which is in contrast to the three-dimensional hydrogen-bonded network observed in **3**.[17,34] The three *tert*-butyl groups bonded to the C3, C22, and C25 atoms are disordered over two positions.

On the other hand, the Rh1−Rh2 and Rh1−Rh2* distances at 180 K in the LT phase are 3.0108(6) and 3.0115(6) Å, respectively (Figure 2c,d); these distances are shortened by ca. 0.084 and 0.020 Å, respectively, compared with those at 240 K. These shortened distances indicate that the order of the shorter and longer Rh−Rh distances in the 1D chain is swapped during the first-order phase transition, which is a tendency similar to the structural phase transition observed for compound **3**. The bond angles of Rh2−Rh1−Rh2* and Rh1−Rh2−Rh1′ are both 171.55(1)°. Similar to the RT phase, eight types of short C···O contacts exist between the neighboring semiquinonato and carbonyl ligands in the stacked molecules (3.005(4)−3.145(5) Å), and these contacts are slightly shortened compared with those in the RT phase. The average C−O distance of the coordinated semiquinonato ligands is 1.312(3) Å, and the six-membered rings also show a quinoid-type distortion: an average of 1.375(5) Å for two alternating short C−C bonds and an average of 1.431(7) Å for four longer C−C bonds. Therefore, **4** in its LT phase is also characterized as a rhodium(I)−semiquinonato complex. The 1,3-propanedioxy groups with the elongated thermal ellipsoids in the RT phase were refined over two sites with 50% occupancy in each atom in the LT phase. Although, in compound **3**, the drastic structural change in the semiquinonato ligands accompanying the exchange of the interchain C−H···O hydrogen-bond partners was observed with the first-order phase transition between 228 and 207 K, compound **4** did not exhibit such a drastic structural change, as shown in Supporting Information Figure S5. Therefore, supercooling was only scarcely observed in the heat capacity measurement because the structural change in **4** is very small. The C···O distances corresponding to the weak C−H···O hydrogen bonds between the 1,3-propanedioxy moieties of adjacent 1D chains are O3···C34A = 3.450(12), O3···C34B = 3.555(14), and O9B···C15 = 3.433(10) Å, respectively (Supporting Information Figures S3 and S4); the adjacent 1D chains in the LT phase are also connected two-dimensionally by the weak C−H···O hydrogen bonds. Another remarkable difference between the crystal structures in the RT and LT phases, as is clearly evident from a comparison of parts a and c of Figure 2, is that the thermal ellipsoids of rhodium and its surrounding coordinated oxygen and carbon atoms in the RT phase are elongated along the 1D chain direction, similar to the case of **3**;[17] this observation is attributed to large-amplitude thermal vibrations of these atoms as this behavior was observed in the RT phase but not in the LT phase.

*[Rh(3,6-DBSQ-4,5-(N,N′-DEN))(CO)$_2$]$_\infty$ (**5**).* Crystal structure analysis of compound **5** was performed at 250 K, and the 1D chain and crystal structures are shown in Figure 3 and Suporting Information Figure S6, respectively. Selected bond lengths are listed in Supporting Information Table S1. Compound **5** crystallizes in triclinic space group $P\bar{1}$. The structure consists of linear chains of planar complex molecules stacked in a staggered arrangement along the *a*-axis, where adjacent molecules are twisted by ca. 144°. The Rh1−Rh2 and Rh1−Rh2′ distances are 2.9662(8) and 3.2266(8) Å, respectively, whose average distance (3.096 Å) is almost the same as those of compounds **3** (3.092 Å)[17] and **4** (3.063 Å); however, the complex molecules in **5** are strongly dimerized in the 1D chain. Bond angles Rh2−Rh1−Rh2′ and Rh1−Rh2−Rh1* are both 179.18(2)°. The average C−O distance of the coordinated dioxolene ligand is 1.316(1) Å, and the six-membered rings also exhibit a quinoid-type distortion: an average of 1.383(8) Å for two alternating short C−C bonds and an average of 1.427(18) Å for four longer C−C bonds. Therefore, compound **5** at 250 K is also characterized as a rhodium(I)−semiquinonato complex. Four and two types of C···O contact distances less than 3.22 Å exist between the

dx.doi.org/10.1021/ic5019532 | *Inorg. Chem.* 2014, 53, 11710−11720

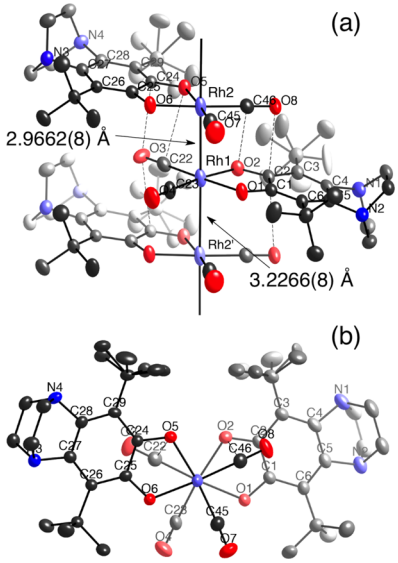

Figure 3. Crystal structure of [Rh(3,6-DBSQ-4,5-(*N*,*N*′-DEN))-$(CO)_2]_\infty$ (**5**) at 250 K. (a) Structure of the infinite chain built from a stack of complex molecules and (b) structural view down the Rh−Rh axis showing an overlap mode of the complex molecules. Symmetry operation: ′ −1+*x*, *y*, *z*. Intermolecular C···O contacts less than the sum of their respective van der Waals radii (3.22 Å) are represented by dashed lines.

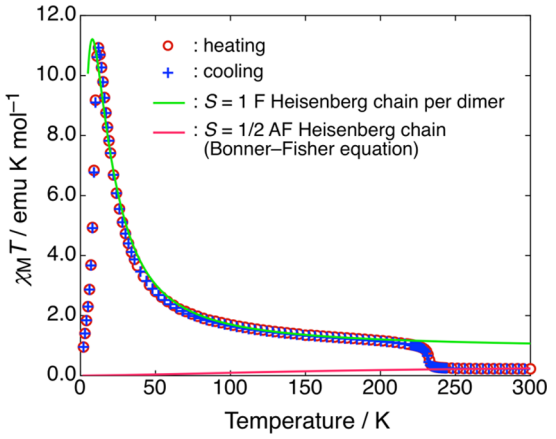

Figure 4. Temperature dependence of the product of the molar magnetic susceptibility and temperature ($\chi_M T$) for [Rh(3,6-DBBQ-4,5-PDO)$(CO)_2]_\infty$ (**4**). The solid lines represent the least-squares fits of the models described in the text to the data.

neighboring semiquinonato and carbonyl ligands in the intra- and interdimer units in the 1D chain, respectively (3.055(7)−3.186(7) Å). The two *tert*-butyl groups bonded to the C3 and C29 atoms are disordered over two positions. In the present compound, the *N*,*N*′-diethylenediamine moieties that protrude vertically from the molecular plane fill the space formed by an overlap of the neighboring semiquinonato and carbonyl ligands. The intermolecular C···N distances between the *N*,*N*′-diethylenediamine moieties of two adjacent 1D chains are relatively short (N4···C42 = 3.553(8) Å), indicating that the two chains are connected by the weak complementary C−H···N hydrogen bonds, as shown in Supporting Information Figure S7.[34]

3.3. Magnetic Properties. *[Rh(3,6-DBSQ-4,5-PDO)-$(CO)_2]_\infty$ (4).* The temperature dependence of the molar magnetic susceptibility (χ_M), which was measured on a polycrystalline sample using a relatively weak static field of 200 Oe to avoid metamagnetism and saturation effects, and the product of the magnetic susceptibility and temperature ($\chi_M T$) are shown in Supporting Information Figure S8 and Figure 4, respectively. The $\chi_M T$ value at 300 K is 0.225 emu K mol^{-1}, which is only two-thirds of the spin-only value of $S = {}^1/_2$ (0.375 emu K mol^{-1}) and is almost constant at temperatures down to ca. 240 K. The $\chi_M T$ values then exhibit an abrupt increase with the first-order phase transition, which is accompanied by a very small thermal hysteresis between 232 and 231 K. As the temperature is decreased in the LT phase, the $\chi_M T$ value drastically increases to a maximum of 10.93 emu K mol^{-1} at 12 K and then decreases rapidly. The rapid increase in the $\chi_M T$ value suggests the presence of a very strong ferromagnetic interaction operating between the semiquinonato radicals of neighboring molecules stacked in the 1D chain. These magnetic behaviors are similar to those observed for **3**;[17] however, compound **4** does not exhibit a large hysteresis because of the absence of a significant structural change with the first-order phase transition. Although the LT phase of **3** exhibits magnetic anisotropy, where the easy axis of magnetization is parallel to the 1D chain direction,[17] the magnetic anisotropy in **4** could not be confirmed because of its small crystal size. The χ_M value also shows a maximum at 11 K and again slightly increases below 5 K upon further cooling (Supporting Information Figure S8). The appearance of the maximum in χ_M is a manifestation of an antiferromagnetic phase transition due to antiferromagnetic coupling between the ferromagnetic 1D chains. The maximum observed in χ_M disappears for $H > 2$ kOe (Supporting Information Figure S9), indicating a field-induced transition from the antiferromagnetic to a ferromagnetic ground state. Furthermore, note that the increase in χ_M observed below 5 K after the antiferromagnetic phase transition suggests the existence of uncompensated residual spin moments.

To evaluate the magnetic interactions of **4** in the RT phase, we tentatively analyzed the magnetic data using the $S = {}^1/_2$ Heisenberg chain models; the details related to their least-squares fittings are described in Supporting Information Figure S10. Although these theoretical equations could not reproduce the experimental data well, the best simulation among them was obtained when the $S = {}^1/_2$ antiferromagnetic (AF) Heisenberg chain model was used (Bonner−Fisher equation, $H = -J\Sigma S_i \cdot S_{i+1}$)[35] (Figure 4). The fitting of the magnetic data between 300 and 260 K leads to $J/k_B = -232(4)$ K, where g is fixed at 2.00 because of the presence of the organic radical. The J/k_B value for **4** is larger than that for **3** ($J/k_B = -163(3)$ K), and the antiferromagnetic interactions are predominant in the overall magnetic interactions in the RT phases of **3** and **4**. The likely reason for the simulation not reproducing the experimental data well is that the next-nearest-neighbor interactions cannot be ignored in the present compound, as previously predicted from DFT calculations of compound **3**.[17]

On the other hand, we attempted to tentatively evaluate the very strong ferromagnetic interactions in the LT phase by using the two theoretical expressions with the Hamiltonian $H = -J\Sigma S_i \cdot S_{i+1}$ with an $S = {}^1/_2$ ferromagnetic (F) Heisenberg chain model (Baker equation)[36] and the half-value of an $S = 1$ ferromagnetic (F) Heisenberg chain model,[37] including the mean-field approximation with zJ',[38] because no theoretical equation is available for an $S = {}^1/_2$ ferromagnetic alternating chain system (Supporting Information Figure S11). Our attempts to fit the magnetic data using the former model

dx.doi.org/10.1021/ic5019532 | *Inorg. Chem.* 2014, 53, 11710−11720

failed; however, the latter model resulted in an excellent fit to the data at temperatures greater than 10 K, with the best-fit parameters being J/k_B = +56(4) K, g = 2.59(7), and zJ'/k_B = −0.45 K (fixed), where the g factor is included in the least-squares fit to consider the magnetic anisotropy observed for compound **3** (Figure 4). This result indicates that the adjacent molecules situated alternately in the chain form the triplet dimers via a very strong ferromagnetic interaction and that the magnetic interaction between the triplet dimers is also ferromagnetic. A similar result based on the ferromagnetic interactions between triplet dimers was obtained for compound **3** (J/k_B = +74(1) K, g = 2.67(2), and zJ'/k_B = −1.98(3) K).[17] The small negative value of zJ'/k_B for **4** indicates that an antiferromagnetic interaction operates between the ferromagnetic 1D chains; its value is smaller than that of **3** (zJ'/k_B = −1.98 K). This difference in the zJ'/k_B values can be attributed to a difference in the dimensionality of interchain hydrogen-bond interactions; the 1D chains in **3** are connected three-dimensionally by the C−H···O hydrogen bonds, whereas the interchain interaction in **4** is two-dimensional. This would lead to a difference in the magnetic behavior below the Néel temperature, as will be discussed later.

To investigate magnetic behaviors of **4** in the LT region, we performed magnetization studies under a weak applied field; the results are shown in Figure 5. The zero-field-cooled

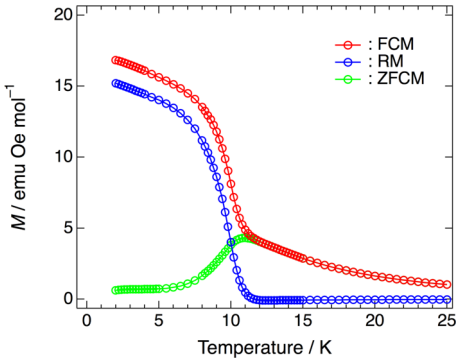

Figure 5. Zero-field-cooled magnetization (ZFCM), field-cooled magnetization (FCM) measured under 5 Oe, and remnant magnetization (RM) for $[Rh(3,6\text{-DBBQ-}4,5\text{-PDO})(CO)_2]_\infty$ (**4**).

magnetization (ZFCM) under a weak applied field of 5 Oe shows a maximum at 10.9 K, whereas the field-cooled magnetization (FCM) shows a rapid increase below a bifurcation point at 12.0 K. Consistent with the thermal irreversibility between ZFCM and FCM below the bifurcation point, a remnant magnetization (RM) of 15.2 emu Oe mol^{-1} is observed after the external magnetic field is turned off at 2 K, and then vanishes at 12.0 K. These results indicate the appearance of a long-range ordering of net magnetic moments in the antiferromagnetic ordered phase, which may originate from the imperfect cancellation of the antiferromagnetically coupled spins between the ferromagnetic 1D chains due to spin canting, the so-called weak ferromagnetism.[39−41]

To further clarify the magnetic ground-state characteristics of **4**, we measured the field-dependent isothermal magnetization at 2 K (Figure 6). The magnetization M first increases slowly with increasing magnetic field, similar to the behavior of a typical antiferromagnet, and then increases abruptly above 1 kOe, implying the onset of a field-induced spin-flip transition from the spin-canting antiferromagnetic phase of the

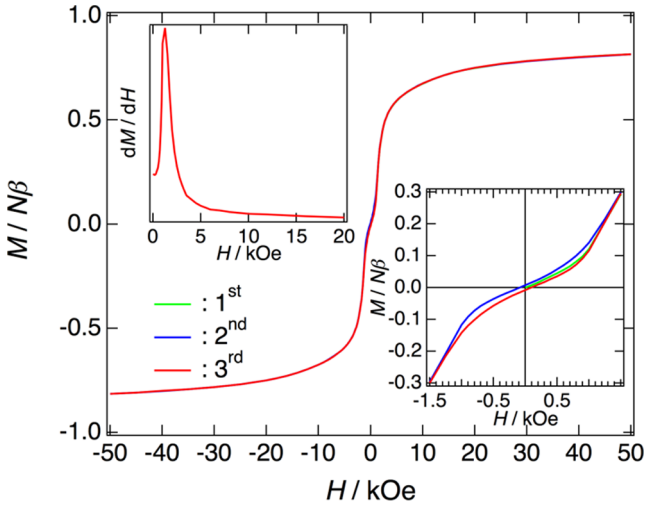

Figure 6. Isothermal field dependence of magnetization M for $[Rh(3,6\text{-DBBQ-}4,5\text{-PDO})(CO)_2]_\infty$ (**4**) measured on a polycrystalline sample at 2 K. The inset in the upper-left corner shows the field dependence of differential magnetization dM/dH. The dM/dH vs H curve shows a peak at 1.25 kOe, which corresponds to the critical field (H_c). The inset in the lower-right corner is an enlarged view that shows the small hysteresis loop between +1.5 and −1.5 kOe.

ferromagnetic chains to a ferromagnetic phase, which is characteristic of a metamagnet.[42] This behavior is also confirmed by the field-dependent magnetization shown in Supporting Information Figure S12. The critical field H_c estimated from the sharp peak in the dM/dH versus H curve is 1.25 kOe. Upon a further increase in the magnetic field above H_c, M increases very slowly and reaches 0.815 $N\beta$ at 50 kOe, which is slightly smaller than the expected saturation magnetization of 1.0 $N\beta$ for S = $^1/_2$ spin. The magnetization M smaller than expected saturation magnetization is probably a result of magnetic anisotropy, as observed for the aligned needle-shaped crystals of compound **3**, where the easy magnetization axis is parallel to the 1D chain direction. The inset of Figure 6 indicates that **4** is a soft magnet displaying a magnetic hysteresis loop with a coercive field of 88 Oe and remnant magnetization of 42 emu Oe mol^{-1} (0.0076 $N\beta$) (Supporting Information Figure S13), and the observed hysteresis is in agreement with the results of the ZFCM, FCM, and RM measurements.

To further elucidate the magnetic behaviors in the LT region, we performed ac susceptibility measurements on a polycrystalline sample in an ac field of 2 Oe oscillating at 1−997 Hz with a zero dc bias field; the results are shown in Figure 7. The in-phase component (χ') exhibits a frequency-independent maximum at 10.9 K, whereas the out-of-phase component (χ'') displays a very weak broad peak centered at 10.2 K, which decreases gradually with increasing frequency. The maximum observed in χ' indicates the occurrence of 3D antiferromagnetic ordering, and the peak temperature corresponds to the Néel temperature, T_N = 10.9 K. The frequency-independent broad peak that appeared in χ'' is not characteristic of an uncanted (collinear) antiferromagnet, but can be explained by the onset of long-range ordering of the canted spins, in agreement with the results of the magnetization studies under a weak applied field and the isothermal magnetization at 2 K.[43,44] Furthermore, below 5.2 K, χ' shows frequency dependence, whereas χ'' starts to display a frequency-dependent peak with a small shoulder. Although the origin of the shoulder is unclear, the frequency-

dx.doi.org/10.1021/ic5019532 | Inorg. Chem. 2014, 53, 11710−11720

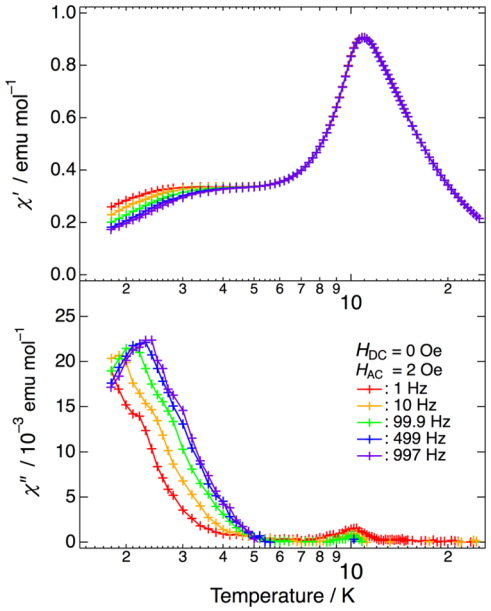

Figure 7. Temperature dependence of the in-phase (χ') and out-of-phase (χ'') components of ac susceptibility for [Rh(3,6-DBBQ-4,5-PDO)$(CO)_2]_\infty$ (**4**) measured on a polycrystalline sample in an ac field of 2 Oe oscillating at 1−997 Hz with a zero dc bias field.

dependent peak is indicative of slow spin relaxation processes, characteristic of spin-glasses, superparamagnets, or single-chain magnets. The frequency dependence of the peak temperature can be measured by the Mydosh parameter ϕ defined by $\phi = (\Delta T_p/T_p)/\Delta(\log 2\pi f)$, where T_p is the peak temperature of the $\chi''(T)$ plot at a certain frequency f. In the case of **4**, ϕ was estimated to be 0.095, which is out of range for a typical spin glass (where ϕ is approximately 0.01)[45] but is close to the normal value for superparamagnets or single-chain magnets ($0.1 \leq \phi \leq 0.3$).[46,47] We estimated the relaxation energy barrier (Δ_τ/k_B) and the characteristic relaxation time (τ_0) by using the Arrhenius law, $\tau = \tau_0 \exp(\Delta_\tau/k_BT)$, leading to Δ_τ/k_B = 51.5 K and $\tau_0 = 2.6 \times 10^{-14}$ s. The value of τ_0 is quite small compared with that of superparamagnets or single-chain magnets,[48,49] excluding the possibility of single-chain magnet behavior. Note that the blocking behavior observed in **4** occurs after the occurrence of 3D AF ordering at T_N = 10.9 K; this behavior is in contrast to the blocking behavior of the individual magnetic moments which first occurs and a long-range ordering which subsequently starts at further lower temperature.[50,51] Taking this observation into account, the slow magnetic relaxation observed in **4** is considered to originate from the movement of magnetic domain walls. The long-range magnetic ordering creates magnetic domains at temperatures near T_N; however, the domain walls can be moved relatively easily because the thermal energy is still sufficient to move them. The domain walls become gradually hard with decreasing temperature. The magnetic relaxations associated with the spin inversions accompanying the domain wall movements by thermal activation subsequently become very slow; as a result, the slow spin relaxation processes can be observed in the ac susceptibility. Similar magnetic relaxations ascribed to the movements of the domain walls have been reported for 1D chain compounds.[50,52−54] On the other hand, such a frequency-dependent peak below the Néel temperature was not observed in the case of compound **3**, possibly because of three-dimensional interchain hydrogen-bond interactions in this compound.[17]

In the case of an anisotropic Heisenberg or Ising-like 1D system, the χT product obtained in the limit of zero field is known to be proportional to the correlation length ξ, and the plot of $\ln(\chi T)$ versus T^{-1} shows a linear component related to the expression $\chi T = C_{eff} \exp(\Delta_\xi/k_BT)$, where C_{eff} is the effective Curie constant and Δ_ξ is the energy necessary to create a domain wall in the chain.[48,55] To examine whether the present compound is 1D by nature, we plotted $\ln(\chi' T)$ versus T^{-1} for the ac measurement results at an ac field of 2 Oe at 1 Hz with zero dc field together with the dc measurements, as shown in Figure 8. The plots of $\ln(\chi T)$ versus T^{-1} for **4** show a linear

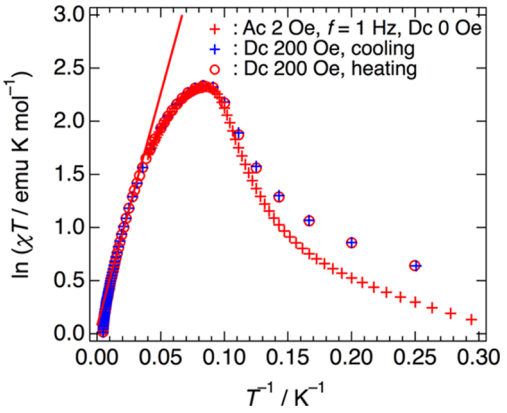

Figure 8. Semilogarithmic plots of χT vs T^{-1} for [Rh(3,6-DBBQ-4,5-PDO)$(CO)_2]_\infty$ (**4**). The data were obtained from the ac measurement with a driving ac field of 2 Oe and 1 Hz under zero dc field and from the dc measurement with a static field of 200 Oe.

part between 84 and 32 K, supporting our hypothesis that the present compound exhibits a one-dimensional nature (anisotropic Heisenberg or Ising-like 1D behavior). By linearly fitting the experimental data using the above equation, we obtained C_{eff} = 1.08 emu K mol^{-1} and Δ_ξ = 43.8(7) K. This magnetic anisotropy is attributable to the contribution of d orbitals of the rhodium ions because the orbital angular momentum of organic radicals disappeared. In general, spin canting arises from magnetic anisotropy and/or an antisymmetric magnetic exchange interaction (i.e., a Dzyaloshinsky−Moriya (DM) interaction), which requires the absence of an inversion center between the interacting magnetic centers.[39,56,57] The DM interaction should also be considered as a possible source of spin canting because no inversion center exists between adjacent semiquinonato ligands. Thus, the observed spin canting is attributable to the magnetic anisotropy and/or the Dzyaloshinsky−Moriya interaction.

*[Rh(3,6-DBSQ-4,5-(N,N′-DEN))$(CO)_2]_\infty$ (**5**).* The temperature dependences of $\chi_M T$ and $\chi_M{}^{-1}$ of **5** measured on a polycrystalline sample under an applied field of 5 kOe are shown in Figure 9. The $\chi_M T$ value of **5** at 300 K is 0.216 emu K mol^{-1}, which is only two-thirds of the spin-only value of $S = {}^1/_2$ (0.375 emu K mol^{-1}). When the temperature is lowered, the $\chi_M T$ value gradually decreases and reaches a minimum of 0.189 emu K mol^{-1} at 152 K. It then slightly increases to a maximum of 0.193 emu K mol^{-1} at 72 K, followed by a rapid decrease to 0.0562 emu K mol^{-1} at 2 K. The fittings of the Curie−Weiss law in the temperature ranges 300−228 K and 152−76 K give C = 0.304 emu K mol^{-1} and θ = −123 K and C = 0.185 emu K mol^{-1} and θ = +5.4 K, respectively. These Curie constants are

dx.doi.org/10.1021/ic5019532 | Inorg. Chem. 2014, 53, 11710−11720

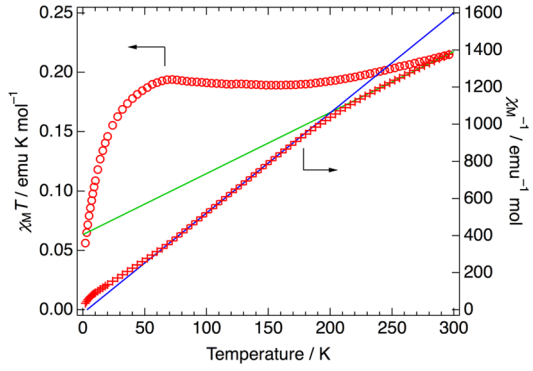

Figure 9. Temperature dependences of $\chi_M T$ and χ_M^{-1} for [Rh(3,6-DBSQ-4,5-(*N*,*N*′-DEN))$(CO)_2]_\infty$ (**5**) measured on a polycrystalline sample under an applied field of 5 kOe. The solid lines represent the least-squares fits of the Curie–Weiss law to the observed data mentioned in the text.

quite smaller than the value expected for an $S = {}^1/_2$ spin. Given the slight increase in $\chi_M T$ with decreasing temperature despite the smaller Curie constant compared with the spin-only value of $S = {}^1/_2$, this complicated magnetic behavior is attributed to a competition between ferromagnetic and antiferromagnetic couplings and/or next-nearest-neighbor interactions, as predicted by the DFT calculations of compound **3**.[17] Therefore, we could not evaluate the magnetic interaction in **5** using a theoretical equation.

3.4. Electronic Absorption Spectra. The UV–vis–NIR–mid-IR spectra of **4** and **5** are shown in Figure 10, together with

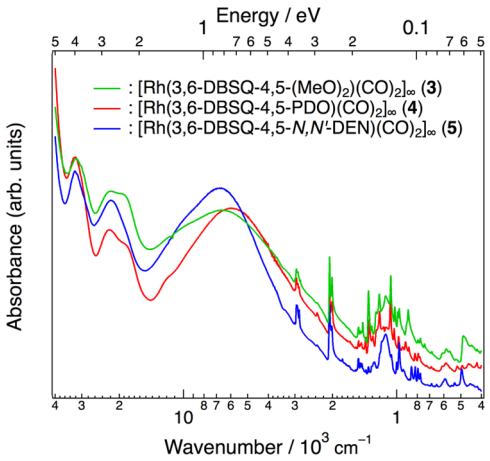

Figure 10. UV–vis–NIR–mid-IR spectra of [Rh(3,6-DBBQ-4,5-PDO)$(CO)_2]_\infty$ (**4**) and [Rh(3,6-DBBQ-4,5-(*N*,*N*′-DEN))$(CO)_2]_\infty$ (**5**) in the solid state (KBr-pressed disk), together with that of [Rh(3,6-DBSQ-$(MeO)_2)(CO)_2]_\infty$ (**3**).[17] The UV–vis–NIR and mid-IR spectra were connected smoothly at approximately 4000–5500 cm^{-1}.

the spectrum of **3**, and the spectral data are summarized in Table 2. An important feature of the spectra of **3**–**5** is the appearance of an intense broad absorption band spread over the NIR and mid-IR spectral regions. The broad absorption band observed in **3** has been attributed to the charge-transfer absorption from a filled 1D d band resulting from axial d_{z^2} orbitals to vacant semiquinonato π^* levels.[17] The more this band expands from the mid-IR to the far-IR region, the more the energy of the electronic excitations decreases; thus, the

Table 2. Electronic Absorption Spectral Data for [Rh(3,6-DBBQ-4,5-PDO)$(CO)_2]_\infty$ (4) and [Rh(3,6-DBBQ-4,5-(*N*,*N*′-DEN))$(CO)_2]_\infty$ (5) in the Solid State, Together with That for [Rh(3,6-DBSQ-$(MeO)_2)(CO)_2]_\infty$ (3)[a,17]

compd	wavenumber/10^3 cm^{-1}
4	5.90, 11.8 (sh), 18.3 (sh), 22.4, 32.3
5	6.70, 9.8 (sh), 21.9, 32.1
3	6.55, 18.9 (sh), 22.1, 31.9

[a]Measured as KBr-pressed disks at 298 K. sh = shoulder.

electrical conductivity is expected to increase. Compound **4** is expected to exhibit a relatively high electrical conductivity despite Rh not being in a mixed-valence state, because the absorption band shows a similar large expanse in the mid-IR region, as observed for **3**. In contrast, for compound **5**, in which complex molecules are strongly dimerized in the 1D chain, the expanse of the absorption band to the mid-IR region is small; therefore, compound **5** is expected to be a poor conductor.

3.5. Electrical Properties. The temperature dependence of the electrical resistivity ρ of compounds **4** and **5** was measured on compressed pellets using a pseudo-four-probe ac method (100 Hz). The results for compound **4** are shown in Figure 11.

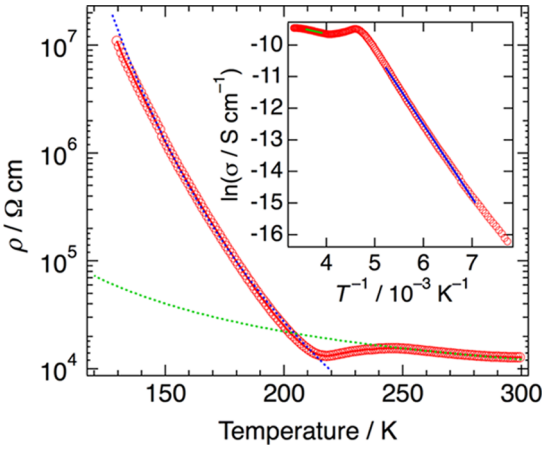

Figure 11. Temperature dependence of the electrical resistivity ρ of [Rh(3,6-DBBQ-4,5-PDO)$(CO)_2]_\infty$ (**4**) measured using a pseudo-four-probe ac method (100 Hz) on a compressed pellet. The inset in the upper-right corner shows the Arrhenius plot of the electrical conductivity σ; these plots were used to determine the activation energy E_a. The dotted lines represent typical semiconductive behaviors in each phase simulated from the Arrhenius law of the electrical conductivity σ.

The electrical conductivity σ of **4** at room temperature is 7.8×10^{-5} S cm^{-1}, which is 1 order of magnitude smaller than that of **3** measured using a single crystal (4.8×10^{-4} S cm^{-1})[17] because it was measured using a compressed pellet. The temperature dependence of the resistivity of **4** in the RT phase exhibits very small temperature dependence and an unusual decrease below a maximum at 245 K before reaching a minimum at 218 K. The unusual decrease observed in the resistivity can be ascribed to the crossover from a semiconductor with a small activation energy of E_a = 31 meV (280–255 K) in the RT phase to a semiconductor with a large activation energy of E_a = 199 meV (192–142 K) in the LT phase, as seen in Figure 11. A similar change in conductive properties from a small thermally activated behavior (E_a = 88 meV) in the RT phase to a relatively large thermally activated behavior (E_a = 386 meV) in

dx.doi.org/10.1021/ic5019532 | *Inorg. Chem.* 2014, 53, 11710–11720

the LT phase has been reported for **3**.[17] A distinct difference between the crystal structures of the RT and LT phases observed for both compounds **3** and **4** is that the thermal ellipsoids of rhodium and its neighboring coordinated atoms in the RT phase are unusually elongated along the 1D chain direction compared with those in the LT phase. This feature can be interpreted as large-amplitude thermal vibrations of these atoms. According to the DFT calculations of **3**, the charge carriers are considered to be generated by the thermal excitation of electrons from a filled 1D d band formed by d_{z^2} orbitals to the lowest unoccupied molecular orbital (LUMO) levels composed of the vacant semiquinonato π^* orbitals (Figure 12a).[17] When a substantial decrease in the Rh−Rh distance accompanies the large-amplitude Rh−Rh vibration, the d band widens and its upper levels are expected to approach the vacant π^* orbitals as shown in Figure 12b. Thus, the thermal excitation of electrons would become easier with decreasing Rh−Rh distance, and unusual conductive behavior would be observed in the RT phase. On the other hand, we could not measure the resistance of compound **5** at room temperature using our LCR meter; therefore, the resistivity is greater than 7×10^7 Ω cm.

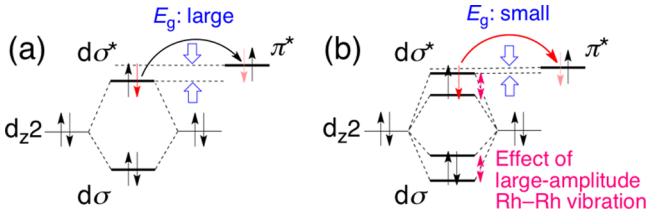

Figure 12. Schematic representations of the energy-level diagrams of filled Rh dσ and dσ* orbitals and a vacant semiquinonato π* orbital. To simplify the thermal excitation of the electron from the upper level of a 1D d band to the semiquinonato π* orbital, the dσ and dσ* orbitals are drawn in this figure instead of the 1D d band. Therefore, the dσ* orbital corresponds to the upper level of the 1D d band. (a) Static model and (b) dynamic model with a large-amplitude Rh−Rh vibration.

4. CONCLUSIONS

To explore the nature of the unusual structural phase transition and magnetic and conductive properties observed in compound **3**, we synthesized two new families of 1D rhodium(I)−semiquinonato complexes, $[Rh(3,6\text{-DBBQ-}4,5\text{-PDO})(CO)_2]_\infty$ (**4**) and $[Rh(3,6\text{-DBBQ-}4,5\text{-}(N,N'\text{-DEN}))(CO)_2]_\infty$ (**5**), and investigated their crystal structures and solid-state properties. Compound **4**, in which the same two ether oxygen atoms as those in **3** are introduced into the semiquinonato ligand (i.e., *O*,*O*-substitutions), underwent a first-order phase transition at T_{trs} = 229.1 K and exhibited a similar change in magnetic properties from antiferromagnetic coupling in the RT phase to strong ferromagnetic coupling in the LT phase. The magnetic behavior of **4** at low temperatures produced a long-range ordering of net magnetic moments originating from the imperfect cancellation of antiferromagnetically coupled spins between the ferromagnetic 1D chain. Furthermore, this compound exhibited an unusual change in thermally activated conductive behavior, from a small activation energy (E_a = 31 meV) in the RT phase to a large activation energy (E_a = 199 meV) in the LT phase, similar to **3**, despite Rh not being in a mixed-valence state. We believe that the shrinkage of the Rh−Rh distance accompanied by the large-amplitude Rh−Rh vibration facilitates the thermal excitation of electrons from a filled 1D d band to the vacant semiquinonato π* orbitals in the RT phase and that this vibronic interaction plays a critical role in the unusual changes in the magnetic and conductive properties observed in **3** and **4**.[58] We are currently verifying this hypothesis. These behaviors are common features exhibited by **3**. However, compound **4** did not exhibit a large hysteresis because its structural change that accompanies the first-order phase transition is small. Furthermore, the χ' and χ'' of **4**, in which interchain interactions (zJ'/k_B = −0.45 K) are weaker than those in **3** (zJ'/k_B = −1.98 K), exhibited a frequency-dependent phenomenon indicating a slow spin relaxation process below 5.2 K; this phenomenon was not observed for **3**, where the 1D chains are connected three-dimensionally by C−H···O hydrogen bonds. The observed slow relaxation process is considered to arise from the movements of the domain walls, as reported for other 1D chain compounds. On the other hand, compound **5**, in which two amino nitrogen atoms are introduced into the semiquinonato ligand (i.e., *N*,*N*-substitutions), showed a fairly short average Rh−Rh distance (3.096 Å), which is almost the same as those of compounds **3** (3.092 Å)[17] and **4** (3.063 Å); however, the complex molecules in **5** are strongly dimerized in the 1D chain. As a consequence, compound **5** did not exhibit unusual magnetic and conductive behaviors such as those exhibited by compounds **3** and **4**.

■ ASSOCIATED CONTENT

Ⓢ Supporting Information

Additional X-ray crystallographic data and magnetic data. This material is available free of charge via the Internet at http://pubs.acs.org.

■ AUTHOR INFORMATION

Corresponding Author

*E-mail: mitsumi@sci.u-hyogo.ac.jp. Fax: (+81) 791-58-0154.

Notes

The authors declare no competing financial interest.

■ ACKNOWLEDGMENTS

This work was financially supported by Grant-in-Aid for Scientific Research (C) (20550130, 24550162) by JSPS, Grant-in-Aid for Scientific Research on Innovative Areas "New Frontier of Materials Science Opened by Molecular Degree of Freedom" (23110723) by MEXT. We also acknowledge the Instrument Center at the Institute for Molecular Science, for the use of a SQUID magnetometer (Quantum Design MPMS-XL7). The synchrotron radiation experiments were performed at the BL02B1 and BL40XU of SPring-8 with the approval of the Japan Synchrotron Radiation Research Institute (JASRI) (Proposals 2006B0095-PU-np/BL02B1 and 2012A1161/BL40XU).

■ REFERENCES

(1) Coronado, E.; Galán-Mascarós, J. R.; Gómez-García, C. J.; Laukhin, V. *Nature* **2000**, *408*, 447−449.
(2) Cui, H.; Wang, Z.; Takahashi, K.; Okano, Y.; Kobayashi, H.; Kobayashi, A. *J. Am. Chem. Soc.* **2006**, *128*, 15074−15075.
(3) Nuida, T.; Matsuda, T.; Tokoro, H.; Sakurai, S.; Hashimoto, K.; Ohkoshi, S.-i. *J. Am. Chem. Soc.* **2005**, *127*, 11604−11605.
(4) Sato, O.; Iyoda, T.; Fujishima, A.; Hashimoto, K. *Science* **1996**, *272*, 704−705.

(5) Hoshino, N.; Iijima, F.; Newton, G. N.; Yoshida, N.; Shiga, T.; Nojiri, H.; Nakao, A.; Kumai, R.; Murakami, Y.; Oshio, H. *Nat. Chem.* **2012**, *4*, 921−926.
(6) Coronado, E.; Martí-Gastaldo, C.; Navarro-Moratalla, E.; Burzurí, E.; Camón, A.; Luis, F. *Adv. Mater.* **2011**, *23*, 5021−5026.
(7) Itkis, M. E.; Chi, X.; Cordes, A. W.; Haddon, R. C. *Science* **2002**, *296*, 1443−1445.
(8) Robertson, C. M.; Myles, D. J. T.; Leitch, A. A.; Reed, R. W.; Dooley, B. M.; Frank, N. L.; Dube, P. A.; Thompson, L. K.; Oakley, a. R. T. *J. Am. Chem. Soc.* **2007**, *129*, 12688−12689.
(9) Robertson, C. M.; Leitch, A. A.; Cvrkalj, K.; Myles, D. J. T.; Reed, R. W.; Dube, P. A.; Oakley, R. T. *J. Am. Chem. Soc.* **2008**, *130*, 14791−14801.
(10) Zhou, B.; Idobata, Y.; Kobayashi, A.; Cui, H.; Kato, R.; Takagi, R.; Miyagawa, K.; Kanoda, K.; Kobayashi, H. *J. Am. Chem. Soc.* **2012**, *134*, 12724−12731.
(11) Lange, C. W.; Földeàki, M.; Nevodchikov, V. I.; Cherkasov, V. K.; Abakumov, G. A.; Pierpont, C. G. *J. Am. Chem. Soc.* **1992**, *114*, 4220−4222.
(12) Nevodchikov, V. I.; Abakumov, G. A.; Cherkasov, V. K.; Razuvaev, G. A. *J. Organomet. Chem.* **1981**, *214*, 119−124.
(13) Pierpont, C. G. *Coord. Chem. Rev.* **2001**, *216*−*217*, 99−125.
(14) Dei, A.; Gatteschi, D.; Sangregorio, C.; Sorace, L. *Acc. Chem. Res.* **2004**, *37*, 827−835.
(15) Sato, O.; Cui, A.; Matsuda, R.; Tao, J.; Hayami, S. *Acc. Chem. Res.* **2007**, *40*, 361−369.
(16) Mitsumi, M.; Goto, H.; Umebayashi, S.; Ozawa, Y.; Kobayashi, M.; Yokoyama, T.; Tanaka, H.; Kuroda, S.-i.; Toriumi, K. *Angew. Chem., Int. Ed.* **2005**, *44*, 4164−4168.
(17) Mitsumi, M.; Nishitani, T.; Yamasaki, S.; Shimada, N.; Komatsu, Y.; Toriumi, K.; Kitagawa, Y.; Okumura, M.; Miyazaki, Y.; Górska, N.; Inaba, A.; Kanda, A.; Hanasaki, N. *J. Am. Chem. Soc.* **2014**, *136*, 7026−7037.
(18) Abakumov, G. A.; Nevodchikov, V. I.; Cherkasov, V. K. *Bull. Acad. Sci. USSR, Div. Chem. Sci.* **1985**, *34*, 2507−2514.
(19) Perrin, D. D.; Armarego, W. L. F. *Purification of Laboratory Chemicals*; Pergamon Press: New York, 1988.
(20) Martinengo, S.; Gxordano, G.; Chini, P.; Parshall, G. W.; Wonchoba, E. R. *Inorg. Synth.* **1990**, *28*, 242−245.
(21) Wheeler, D. E.; McCusker, J. K. *Inorg. Chem.* **1998**, *37*, 2296−2307.
(22) Abakumov, G. A.; Cherkasov, V. K.; Kocherova, T. N.; Druzhkov, N. O.; Kurskii, Y. A.; Bubnov, M. P.; Fukin, G. K.; Abakumova, L. G. *Russ. Chem. Bull.* **2007**, *56*, 1849−1856.
(23) Prokof'eva, T. I.; Vol'eva, V. B.; Prokof'ev, A. I.; Belostotskaya, S.; Komissarov, N. L.; Ershov, V. V. *Chem. Heterocycl. Compd.* **2000**, *36*, 923−930.
(24) Kume, Y.; Miyazaki, Y.; Matsuo, T.; Suga, H. *J. Phys. Chem. Solids* **1992**, *53*, 1297−1304.
(25) DENZO and SCALEPACK: Otwinowski, Z.; Minor, W. *Methods Enzymol.* **1997**, *276*, 307−326.
(26) PLATON: Spek, A. L. *J. Appl. Crystallogr.* **2003**, *36*, 7−13.
(27) Yasuda, N.; Murayama, H.; Fukuyama, Y.; Kim, J.; Kimura, S.; Toriumi, K.; Tanaka, Y.; Moritomo, Y.; Kuroiwa, Y.; Kato, K.; Tanaka, H.; Takata, M. *J. Synchrotron Radiat.* **2009**, *16*, 352−357.
(28) Yasuda, N.; Fukuyama, Y.; Toriumi, K.; Kimura, S.; Takata, M. *AIP Conf. Proc.* **2010**, *1234*, 147−150.
(29) SIR97: Altomare, A.; Burla, M. C.; Camalli, M.; Cascarano, G. L.; Giacovazzo, C.; Guagliardi, A.; Moliterni, A. G. G.; Polidori, G.; Spagna, R. *J. Appl. Crystallogr.* **1999**, *32*, 115−119.
(30) Sheldrick, G. M. *Acta Crystallogr.* **2008**, *A64*, 112−122.
(31) Yadokari-XG: Wakita, K. *Software for Crystal Structure Analyses*; 2001.
(32) Kabuto, C.; Akine, S.; Nemoto, T.; Kwon, E. *J. Crystallogr. Soc. Jpn.* **2009**, *51*, 218−224.
(33) Adams, D. M.; Dei, A.; Rheingold, A. L.; Hendrickson, D. N. *Angew. Chem., Int. Ed.* **1993**, *32*, 880−882.
(34) Gilli, G.; Gilli, P. *The Nature of the Hydrogen Bond, Outline of a Comprehensive Hydrogen Bond Theory*; Oxford University Press: Oxford, U.K., 2009.
(35) Estes, W. E.; Gavel, D. P.; Hatfield, W. E.; Hodgson, D. J. *Inorg. Chem.* **1978**, *17*, 1415−1421.
(36) Baker, G. A.; Rushbrooke, G. S.; Gilbert, H. E. *Phys. Rev.* **1964**, *135*, A1272−A1277.
(37) Fisher, M. E. *Am. J. Phys.* **1964**, *32*, 343−346.
(38) O'Connor, C. J. *Prog. Inorg. Chem.* **1982**, *29*, 203−283.
(39) Carlin, R. L. *Magnetochemistry*; Springer-Verlag: Berlin, 1986.
(40) Kahn, O. *Molecular Magnetism*; VCH Publishers: New York, 1993.
(41) Weng, D.-F.; Wang, Z.-M.; Gao, S. *Chem. Soc. Rev.* **2011**, *40*, 3157−3181.
(42) Numata, Y.; Inoue, K.; Baranov, N.; Kurmoo, M.; Kikuchi, K. *J. Am. Chem. Soc.* **2007**, *129*, 9902−9909.
(43) Yee, G. T.; Whitton, M. J.; Sommer, R. D.; Frommen, C. M.; Reiff, W. M. *Inorg. Chem.* **2000**, *39*, 1874−1877.
(44) Wang, G.; Slebodnick, C.; Butcher, R. J.; Tam, M. C.; Crawford, T. D.; Yee, G. T. *J. Am. Chem. Soc.* **2004**, *126*, 16890−16895.
(45) Mydosh, J. A. *Spin Glasses: An Experimental Introduction*; Taylor & Francis: London, 1993.
(46) Wang, Y.-Q.; Zhang, X.-M.; Li, X.-B.; Wang, B.-W.; Gao, E.-Q. *Inorg. Chem.* **2011**, *50*, 6314−6322.
(47) David, R.; Kabbour, H.; Colis, S.; Mentré, O. *Inorg. Chem.* **2013**, *52*, 13742−13750.
(48) Coulon, C.; Miyasaka, H.; Clérac, R. *Struct. Bonding (Berlin)* **2006**, *122*, 163−206.
(49) Sun, H.-L.; Wang, Z.-M.; Gao, S. *Coord. Chem. Rev.* **2010**, *254*, 1081−1100.
(50) Ishii, N.; Okamura, Y.; Chiba, S.; Nogami, T.; Ishida, T. *J. Am. Chem. Soc.* **2008**, *130*, 24−25.
(51) Miyasaka, H.; Nakata, K.; Lecren, L.; Coulon, C.; Nakazawa, Y.; Fujisaki, T.; Sugiura, K.-i.; Yamashita, M.; Clérac, R. *J. Am. Chem. Soc.* **2006**, *128*, 3770−3783.
(52) Minguet, M.; Luneau, D.; Lhotel, E.; Villar, V.; Paulsen, C.; Amabilino, D. B.; Veciana, J. *Angew. Chem., Int. Ed.* **2002**, *41*, 586−589.
(53) Oka, Y.; Inoue, K.; Kumagai, H.; Kurmoo, M. *Inorg. Chem.* **2013**, *52*, 2142−2149.
(54) Ishida, T.; Okamura, Y.; Watanabe, I. *Inorg. Chem.* **2009**, *48*, 7012−7014.
(55) Zhang, W.-X.; Ishikawa, R.; Breedlove, B.; Yamashita, M. *RSC Adv.* **2013**, *3*, 3772−3798.
(56) Dzyaloshinsky, I. *J. Phys. Chem. Solids* **1958**, *4*, 241−255.
(57) Moriya, T. *Phys. Rev.* **1960**, *120*, 91−98.
(58) Mitsumi, M.; Murase, T.; Kishida, H.; Yoshinari, T.; Ozawa, Y.; Toriumi, K.; Sonoyama, T.; Kitagawa, H.; Mitani, T. *J. Am. Chem. Soc.* **2001**, *123*, 11179−11192.